Turkish Journal of Civil Engineering, 2026, xxxx-xxxx, Paper xxx, ***Research Article***

Effect of Composite Gravity Framing on Seismic Response of Eccentrically Braced Frames

Mehmet Bakır BOZKURT[1*]
Michael D. ENGELHARDT[2]

ABSTRACT

This paper presents a numerical study investigating the effect of composite gravity frames (CGFs) on the seismic response of eccentrically braced frames (EBFs) subjected to a suite of earthquake ground motions. Two different modeling approaches were considered for each archetype with 4, 8, and 16 stories. While the first model included only the bare steel EBF, the second model considered the EBF together with tributary gravity frames (GFs) and included the effects of a composite floor slab both on the response of the gravity frame connections and on the response of EBF links. A total of 1056 nonlinear time-history analyses were performed using the Opensees software by subjecting the archetypes to 44 scaled and unscaled far-field ground motions defined in FEMA P695. Interstory drift ratios, residual drift ratios, link rotation angles and residual link rotation angles were considered as the response indicators. In addition, a process of removing damaged links was simulated to evaluate the amount of residual drift after this process. The analyses show that the CGFs have a significant beneficial effect on the performance of EBF in terms of link rotation angles and residual drift ratios. Further, the process of removing links for replacement may provide additional benefits in allowing further reductions in residual drift ratio obtained as less than 0.5% even under ground motions scaled to the maximum considered earthquake when the CGFs were included in the model.

Keywords: Eccentrically braced frame, gravity frame, composite slab, residual drift, residual link rotation angles.

1. INTRODUCTION

Eccentrically braced frames (EBFs) are a steel lateral load resisting systems used for seismic resistance. The link members, which are the main source of energy dissipation, are expected

Note:
- This paper was received on June 25, 2025 and accepted for publication by the Editorial Board on November 7, 2025.
- Discussions on this paper will be accepted by xxxxxxx xx, xxxx.
- https://doi.org/

1 Manisa Celal Bayar University, Department of Civil Engineering, Manisa, Türkiye
mehmet.bozkurt@cbu.edu.tr - https://orcid.org/0000-0002-1213-3092

2 The University of Texas at Austin, Department of Civil, Arc. and Env. Eng., Austin, TX 78712, USA
mde@mail.utexas.edu - https://orcid.org/0000-0001-5868-196X

* Corresponding author

to yield under seismic loads, and all other structural members are designed to remain essentially elastic. The yielding mechanism of the links is based on the link length ratio, $\rho = e/(M_p/V_p)$, where e is the link length, and M_p and V_p are the plastic moment and plastic shear capacity of the link respectively. According to AISC 341-22 [1], short links with $\rho \leq 1.6$ yield primarily in shear whereas long links with $\rho \geq 2.6$ yield primarily in flexure. Links having $1.6 < \rho < 2.6$ yield under the simultaneous action of shear and flexure. In the scope of this research, only shear links ($\rho \leq 1.6$) were addressed because shear links generally provide for the best overall seismic performance of EBFs [2]. A detailed literature review on EBFs is provided by Kazemzadeh Azad and Topkaya [2].

Buildings constructed using EBFs were subject to strong ground motions in the New Zealand earthquakes in 2010 and 2011. Clifton et al. [3, 4] reported that EBFs showed good performance although some links fractured due to improperly located link stiffeners. Damaged links were replaced in some buildings [5, 6]. The replacement process was rather difficult because links and collector beams were fabricated as a continuous member, as is the typical practice for EBFs. In order to circumvent this difficulty, researchers have proposed replaceable links that are connected to the adjoining structural members with end plates [7-9], extended end plates [10-13], web connections [11, 12], direct brace attachments [14, 15], and gusseted brace attachments [14, 16]. Replaceable links using extended end plate connections were implemented in the repair of a 22-story EBF in New Zealand following the 2010-11 earthquake sequence [6], marking one of the first applications of replaceable links in practice.

One of the important parameters affecting the cost and feasibility of repairs following a seismic event is the residual drift of the damaged building. McCormick et al. [17] proposed that the residual drift of the structures should be lower than 0.5% to maintain functionality, construction tolerances, and safety and to avoid occupant discomfort. Detachable shear links proposed by Bozkurt et al. [18] and mid-spliced end-plated replaceable links proposed by Özkılıç et al. [19] were developed to facilitate replacement of the damaged links in buildings with residual drift ratios of 0.5% to 0.7%. Residual drift ratios of EBFs were reported as 0.14% for a 12-story building [4] and 0.3% for a 22-story building [6] after the New Zealand earthquakes in 2010 and 2011. These small residual drifts were attributed, in part, to the contribution of out-of-plane rigidity of the composite slab [4, 6] at the EBF links.

Several researchers have shown that gravity frames (GFs) contribute to increased lateral stiffness [20] and reduced lateral displacement [21] of buildings. Typical beam-to-column connections used in gravity framing (shear tabs, double angles, etc.) are generally modeled as pinned connections for design purposes. However, several researchers have shown that these gravity framing connections can provide significant rotational stiffness, strength, and ductility, especially when the effects of a composite floor slab are considered [22, 23, 24, 25]. The contribution of the gravity framing connections combined with the contribution of gravity frame column continuity can result in a reduction of residual drift [26, 27].

In analytical and experimental studies, damaged structures were observed to come back close to their initial position in the process of replacement of the damaged links in a dual system where high-strength moment resisting frames (MRFs) and EBFs were used together [9, 28, 29, 30, 31]. In the DUAREM project [31] where a three-story three-bay structure was subjected to pseudo-dynamic loading at different performance levels, residual frame drifts of

0.09% and 0.14% were reported for damage limitation and significant damage performance levels respectively.

As noted earlier, buildings with EBFs after the New Zealand earthquakes in 2010 and 2011 showed small levels of residual drift. [4, 6]. On the other hand, the reason for the unexpectedly low residual drifts of buildings with EBFs has not been demonstrated by numerical analysis. Although residual drift performance of moment resisting frames and buckling restrained braced frames have been studied in detail [32], less is known about the residual drift performance of EBFs. Furthermore, the effects of the composite gravity frames (CGFs) on the seismic performance of the EBF, and in particular, on the residual drifts of EBFs, have not been reported in any of the studies carried out to date.

A numerical study was undertaken to investigate the effect of CGFs on seismic performance of EBFs after a seismic event and re-centering capability after the link removal process. Six archetypes defined in NIST Technical Note 1863-3 [33] were considered. Two numerical models, referred to herein as Model A and as Model B were created separately to investigate the contribution of CGFs composed of GFs and the out-of-plane rigidity of the composite slab to the seismic response of EBFs. Scaled and unscaled ground motions were also considered in this study. Interstory drift ratios, residual drift ratios, link rotation angles, and residual link rotation angles under different ground motions were quantified. The re-centering capability of EBFs after the removal of damaged links was studied through the same numerical models and is presented herein. Moreover, the reason of the small level of residual drifts was examined in detail.

In this study, a total of 1056 nonlinear time-history analyses were performed by using the Opensees [34] software. Archetypes having 4, 8 and 16 stories were subjected to 44 scaled and unscaled far-field ground motion records defined in FEMA P695 [35]. Ground motions were scaled based on a risk-targeted maximum considered earthquake (MCE_R). The seismic design category, site class, and risk category were selected as D_{max}, D and II respectively. The seismic response of the EBFs designed based on equivalent lateral force (ELF) and response spectrum analysis (RSA) were also compared.

2. DESIGN DETAILS OF THE ARCHETYPES

In this study, the archetypes with 4, 8 and 16 stories defined in NIST Technical Note 1863-3 [33] were considered and are referred to as ME4, ME8 and ME16. In the design by NIST, seismic forces were calculated based both on ELF and on RSA procedures defined in ASCE 7-10 [36] separately. Although ASCE 7-10 [36] does not allow ELF to be used for the design of the 16 story building, it is included in this study for comparative purposes, as it was in the NIST study [33]. Note that ASCE 7-22 now allows ELF for all buildings, and would therefore allow ELF for the design of ME16.

Plan dimensions of all archetype buildings are 45.7m (150') by 30.5m (100') as indicated in Figure 1. The height of the first story is 5.5m (18') whereas the remainder of the stories have a height of 4.3m (14') for all archetypes. Seismic loads acting on the archetypes are carried by moment resisting frames in the x-direction and EBFs in the y-direction. In the scope of this study, only the y-direction of the building is considered. The bay width of the EBFs is 6.1m (20') for ME4 and ME8, and 9.1m (30') for ME16. The link length is 762mm (30") for

ME4 and ME8, and is 991mm (39") for ME16. The link length ratio, $\rho = e/(M_p/V_p)$, varies between 0.81 and 1.59 and therefore all links are classified a shear links ($\rho \leq 1.6$). The e/L ratio varies between 0.108 and 0.125. The e/L ratio, which is the ratio of link length to bay width, affects the relationship between story drift ratio and link rotation angle [2]. All structural members in the EBFs are connected to each other using rigid connections. In the CGFs, beams are assumed to be connected to columns using shear tab connections. Column bases are modeled as fixed supports in the EBFs and as pin supports in the CGFs. A plan view of the archetypes and an elevation view of ME8 are shown in Figures 1 and 2 respectively. Steel sections used in the EBFs and the CGFs are listed in Tables 1 and 2 respectively.

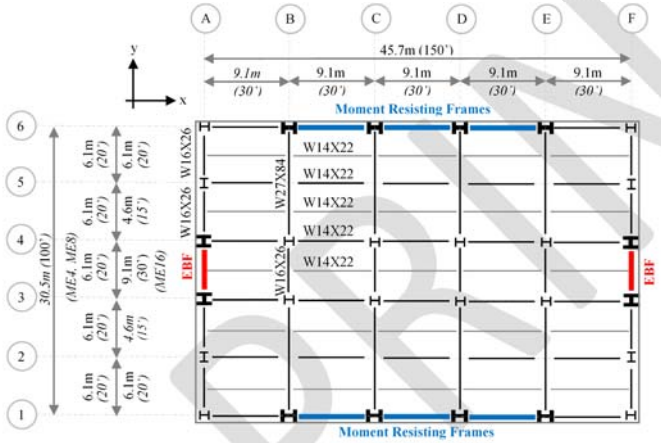

Figure 1 - Typical floor plan of archetypes defined in NIST Technical Note 1863-3 [33]

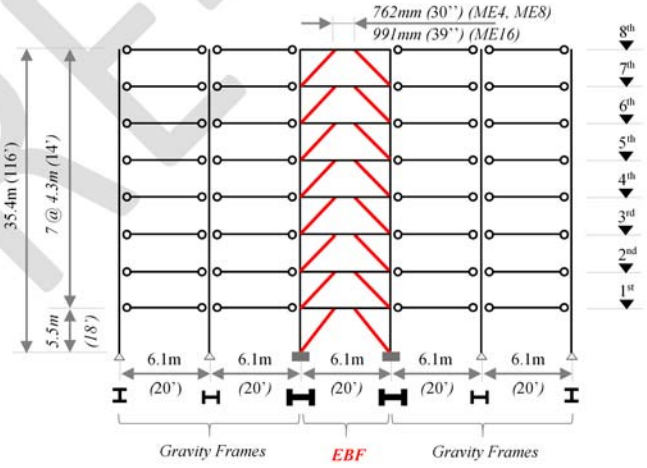

Figure 2 - Elevation view of ME8 defined in NIST Technical Note 1863-3 [33]

The orientation of GCs in steel structures is generally governed by architectural constraints and the alignment with the primary lateral load-resisting systems to ensure structural efficiency. In the presented study, they are oriented parallel to the direction of the lateral resisting frames when such systems are present, whereas in frames without dedicated lateral systems, they are aligned with the direction of the moment-resisting frames to maintain structural consistency. Therefore, as shown in Figure 1, all columns of the CGFs except those at A-2, A-5, F-2 and F-5 are oriented for weak-axis bending in the y-direction of the building.

Table 1: Steel sections in EBFs [33]

A	*S*	EBF designed based on ELF				EBF designed based on RSA			
		Column	Beam and Link	Brace	$\frac{e}{\left(\frac{M_p}{V_p}\right)}$	Column	Beam and Link	Brace	$\frac{e}{\left(\frac{M_p}{V_p}\right)}$
ME4	4	W14x48	W14x26	HSS6x1/2	1.49	W14x48	W14x26	HSS6x6x1/2	1.49
	3	W14x48	W14x38	HSS6x1/2	1.19	W14x48	W14x38	HSS6x6x1/2	1.19
	2	W14x132	W16x50	HSS8x1/2	1.12	W14x132	W16x45	HSS7x7x1/2	1.13
	1	W14x132	W16x89	HSS9x1/2	0.81	W14x132	W16x77	HSS8x8x1/2	0.82
ME8	8	W14x82	W14x26	HSS6x1/2	1.49	W14x148	W14x26	HSS6x6x1/2	1.49
	7	W14x82	W14x38	HSS6x1/2	1.19	W14x148	W14x26	HSS6x6x1/2	1.49
	6	W14x132	W16x45	HSS7x1/2	1.13	W14x68	W16x31	HSS6x6x5/8	1.38
	5	W14x132	W18x55	HSS7x5/8	1.06	W14x68	W16x40	HSS6x6x5/8	1.13
	4	W14x159	W18x60	HSS7x5/8	1.02	W14x132	W18x40	HSS7x7x1/2	1.22
	3	W14x159	W21x57	HSS8x5/8	1.12	W14x132	W18x46	HSS7x7x5/8	1.21
	2	W14x211	W21x57	HSS9x5/8	1.12	W14x145	W18x55	HSS8x8x1/2	1.06
	1	W14x211	W21x83	HSS9x5/8	0.93	W14x145	W21x83	HSS9x9x5/8	0.93
ME16	16	W14x74	W14x48	W12x58	1.28	W14x48	W14x38	W12x58	1.54
	15	W14x74	W14x48	W12x58	1.28	W14x48	W14x38	W12x58	1.54
	14	W14x176	W18x40	W12x72	1.58	W14x82	W14x38	W12x58	1.54
	13	W14x176	W18x40	W12x72	1.58	W14x82	W14x38	W12x58	1.54
	12	W14x193	W18x55	W12x79	1.37	W14x132	W14x38	W12x72	1.54
	11	W14x193	W18x60	W12x79	1.33	W14x132	W16x45	W12x72	1.47
	10	W14x283	W21x57	W12x87	1.45	W14x159	W18x50	W12x87	1.39
	9	W14x283	W21x68	W12x87	1.24	W14x159	W18x55	W12x87	1.37
	8	W14x370	W21x73	W12x87	1.22	W14x233	W21x50	W12x87	1.59
	7	W14x370	W21x83	W12x96	1.21	W14x233	W21x62	W12x87	1.29
	6	W14x455	W21x83	W12x96	1.21	W14x283	W21x68	W12x87	1.24
	5	W14x455	W21x83	W12x96	1.21	W14x283	W21x68	W12x87	1.24
	4	W14x550	W21x83	W12x96	1.21	W14x342	W21x73	W12x96	1.22
	3	W14x550	W21x83	W12x96	1.21	W14x342	W21x73	W12x96	1.22
	2	W14x665	W21x83	W12x96	1.21	W14x426	W21x73	W12x96	1.22
	1	W14x665	W24x103	W12x120	1.04	W14x426	W24x103	W12x120	1.04

A: archetypes, *S*: story number

Table 2: Steel sections in gravity frames

A	*S*	Columns					Beams	
		2-A, 5-A	1-A, 6-A	1-B, 6-B	1-C, 6-C	3-B, 4-B 3-C, 4-C	A-1,3 A-4,6 B-3,4 C-3,4	B-1,3 B-4,6 C-1,3 C-4,6
ME4	4	W12x35	W12x26	W14x132	W14x193	W12x40	W16x26	W27x84
	3	W12x35	W12x26	W14x132	W14x193	W12x40	W16x26	W27x84
	2	W12x50	W12x35	W14x132	W14x193	W12x72	W16x26	W27x84
	1	W12x50	W12x35	W14x132	W14x193	W12x72	W16x26	W27x84
ME8	8	W12x40	W12x26	W18x55	W18x119	W12x40	W16x26	W27x84
	7	W12x40	W12x26	W18x55	W18x119	W12x40	W16x26	W27x84
	6	W12x45	W12x30	W18x71	W18x143	W12x65	W16x26	W27x84
	5	W12x45	W12x30	W18x71	W18x143	W12x65	W16x26	W27x84
	4	W12x53	W12x40	W18x106	W18x192	W12x96	W16x26	W27x84
	3	W12x53	W12x40	W18x106	W18x192	W12x96	W16x26	W27x84
	2	W12x65	W12x50	W18x175	W18x192	W12x136	W16x26	W27x84
	1	W12x65	W12x50	W18x175	W18x192	W12x136	W16x26	W27x84
ME16	16	W12x40	W12x26	W27x94	W27x129	W12x40	W16x26	W27x84
	15	W12x40	W12x26	W27x94	W27x129	W12x40	W16x26	W27x84
	14	W12x45	W12x30	W27x114	W27x129	W12x65	W16x26	W27x84
	13	W12x45	W12x30	W27x114	W27x129	W12x65	W16x26	W27x84
	12	W12x53	W12x35	W27x114	W27x235	W12x87	W16x26	W27x84
	11	W12x53	W12x35	W27x114	W27x235	W12x87	W16x26	W27x84
	10	W12x53	W12x40	W27x146	W27x235	W12x120	W16x26	W27x84
	9	W12x53	W12x40	W27x146	W27x235	W12x120	W16x26	W27x84
	8	W12x65	W12x40	W27x161	W27x281	W12x152	W16x26	W27x84
	7	W12x65	W12x40	W27x161	W27x281	W12x152	W16x26	W27x84
	6	W12x72	W12x50	W27x194	W27x281	W12x170	W16x26	W27x84
	5	W12x72	W12x50	W27x194	W27x281	W12x170	W16x26	W27x84
	4	W12x79	W12x53	W27x235	W27x368	W12x210	W16x26	W27x84
	3	W12x79	W12x53	W27x235	W27x368	W12x210	W16x26	W27x84
	2	W12x96	W12x65	W27x336	W27x368	W12x252	W16x26	W27x84
	1	W12x96	W12x65	W27x336	W27x368	W12x252	W16x26	W27x84

A: archetypes, *S*: story number

According to NIST Technical Note 1863-3 [33], dead loads that do not include self-weight are taken as 2.20 kPa (46 psf) for the floors and 0.72 kPa (15 psf) for the roof. Live loads are taken as 2.39 kPa (50 psf) for the floors and 1.44 kPa (30 psf) for the roof. Moreover, a 3.65 kN/m (250 plf) dead load is applied along the perimeter of the archetypes for the façade load.

As seen in Table 1, member sizes are generally heavier in the EBFs designed using ELF compared to those designed by RSA. Natural periods in the y-direction of ME4, ME8 and ME16 designed based on ELF are 1.08, 2.09 and 3.11 sec whereas those based on RSA are 1.14, 2.38 and 3.68 sec respectively. This indicates the EBFs designed using ELF are somewhat stiffer than those designed using RSA.

Wide flange steel sections made of ASTM A992 grade steel with a specified yield strength of 50 ksi (345 MPa) were used in the columns and beams of all archetypes and in the braces of ME16. Square hollow structural sections made of ASTM A500 grade B steel with a specified yield strength of 46 ksi (317 MPa) were used in the braces of ME4 and ME8. All members in the EBFs and all beams in the CGFs were taken directly from NIST Technical Note 1863-3 [33]. Columns sizes in the CGFs were not reported in NIST Technical Note 1863-3 [33]. Consequently, the column sizes in the CGFs were established based on AISC 360-10 [37] as a part of this research using the dead and live loads noted earlier. In the design of the CGFs, live load reduction factors were not taken into consideration.

3. NUMERICAL MODELING

Nonlinear time-history analyses were carried out using Opensees [34]. The damping ratio of the structure was taken as 0.02. Columns, beams, and braces were modeled by using the "nonlinearBeamColumn" element to take into account nonlinear inelastic behavior along the length of the members. The "Steel02 material- Giuffré-Menegotto-Pinto model with isotropic strain hardening" nonlinear material model was selected. A strain hardening ratio of $b = 0.02$, and parameters which control the transition from elastic to inelastic behavior of $R0 = 20$, $CR1 = 0.925$, and $CR2 = 0.15$ were used. In modeling the link members, the "beamWithHinges" elements providing plastic hinges at the member ends were used. To simulate a shear hinge, the three translational springs proposed by Ramadan and Ghobarah [38] were assembled at each end of the link as illustrated in Figure 3.

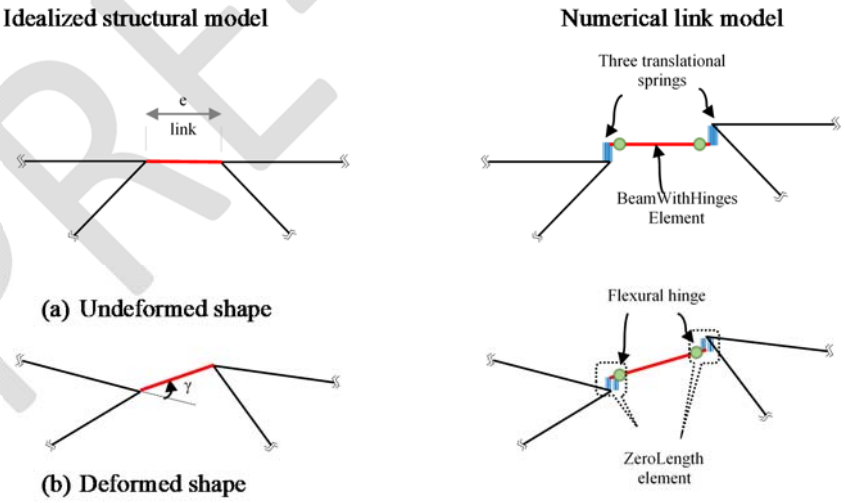

Figure 3 - Details of numerical link model

"ZeroLength" elements were used to combine the three translational springs simulating a shear hinge with the rotational springs simulating flexural hinges. The rotational spring coefficient was defined based on the plastic moment capacity of the link. Since this research covers only shear links, flexural hinges were not expected to occur at the ends of the links. The stiffness of the springs simulating the shear hinge of the link was chosen based on the coefficients recommended by Richards and Uang [39] as shown in Figure 4. The stiffness of the springs was further modified to take into consideration the effect of the composite slab on the seismic behavior of the link. Details of this modification are discussed later.

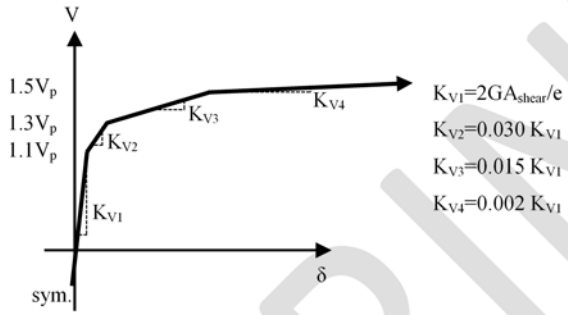

Figure 4 - Stiffness coefficients of the link proposed by Richards and Uang [39]

The Opensees [34] numerical models were validated based on experimental data for shear links. Specifically, specimens 4A, 8, 10, 4A-RLP, 8-RLP and 10-RLP reported by Okazaki et al. [40] with a link length ratio, ρ varying between 1.04 and 1.49 were considered. Specimens 4A, 8 and 10 were subjected to the loading protocol defined in AISC341-02 [41] whereas the others were subjected to the loading protocol defined in AISC341-05 [42]. In order to compare numerical and experimental results, the test setup used by Okazaki et al. [40] was modeled on Opensees [34]. Comparisons of link shear force versus link rotation angle response obtained from numerical models and experimental data are shown Figure 5. The link numerical model did not include the Bauschinger effect, resulting in some differences in the loading and unloading responses compared to the experiments. Still, shear forces on the link members corresponding to the link rotation angle at each cycle obtained from numerical modeling are well-matched with the values obtained from experimental results. Note that the numerical model for the links did not include simulation of link fracture. Experiments have shown that well designed and detailed shear links can sustain rotation angles on the order of ± 0.10 to ± 0.12 rad prior to fracture [40].

Two different numerical models were developed for each archetype. These are referred to as Model A and Model B. Model A only includes the bare steel EBF. Model B includes both the EBF and the tributary CGFs. For the CGFs, the models of the beam-to-column connections include the influence of the composite floor slab on the connection response. Model B also includes the influence of the composite floor slab on the link response. Both numerical models consider only 2-dimensional response and both have leaning columns connected to the EBF using truss members to take into account the *P-Δ* effect of the gravity load tributary to the EBF. Since there are two EBFs in the y-direction, only half of the vertical

loads acting on floors were applied to the nodes of these leaning columns at each floor level. On the other hand, the seismic mass of the archetypes was applied at the joints of the beam-to-column connections of the EBF at each floor level.

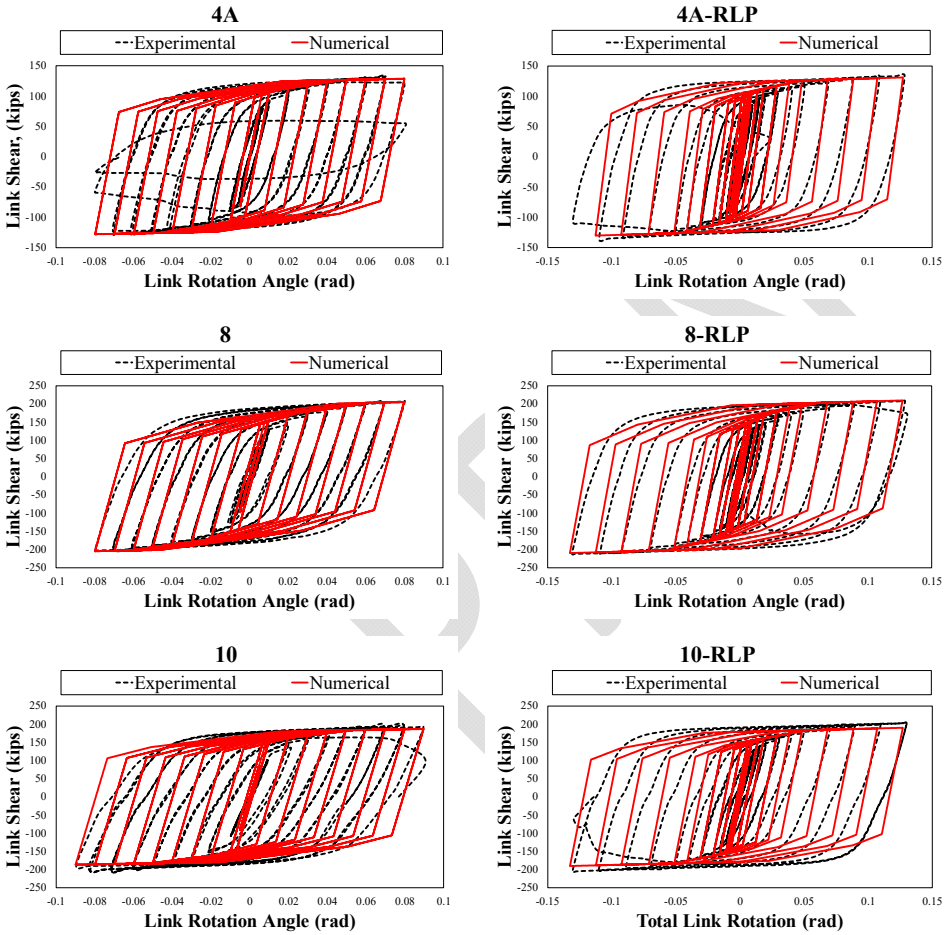

Figure 5 - Comparison of the numerical models and experimental results of the shear links conducted by Okazaki et al. [40]

As shown in Figure 6, to define the contribution of the CGFs to the seismic response of the structure, the CGFs were modeled in addition to the EBF. There are six frame lines in the y direction, two of which have EBFs. One frame line with an EBF and CGFs, and two frame lines of gravity framing only were included in the 2-dimensional model, as shown in Figure 6. These frames were connected to each other by using truss members.

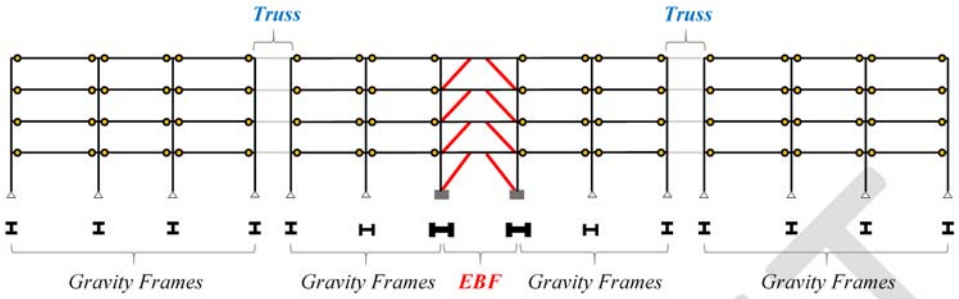

Figure 6 - Numerical modeling of the gravity frames and EBF in Model B

The "NonlinearBeamColumn" element was utilized for beams and columns in the CGFs and the "modified Ibarra-Medina-Krawinkler Deterioration Model with Pinched Hysteretic Response" was utilized to simulate rotational response of the beam-to-column connections in the CGFs including the effects of the composite floor slab. In these connections, positive and negative effective yielding strengths, M^{+}_{slip} and M^{-}_{slip} were taken 25% and 15% of the yield moment of the beams at the connection. The strain hardening coefficient in this model was taken as 0.075, plastic rotation capacities corresponding to the maximum moment capacity for positive and negative loading directions were taken 0.02 rad and 0.01 rad and those corresponding to the ultimate moment capacity for positive and negative loading directions were taken as 0.04 rad and 0.01 rad respectively. The ratio of the force at which reloading begins to the force corresponding to the maximum previous demand in both positive and negative loading direction, Fpr was taken 0.20. Both basic strength deterioration and post-capping strength deterioration known as cyclic strength deterioration were modeled by translating the two strength bounds proposed by Lignos and Krawinkler [43]. Overall, the maximum moment capacities of the beam to column connections in the CGFs vary between $0.32xM_p$ and $0.42xM_p$ for positive bending and $0.15xM_p$ and $0.23xM_p$ for negative bending. Furthermore, the moment capacity drops to zero for both loading directions at large rotations. The moment rotation relationship from this numerical model was compared with specimen 3A having a composite slab from the experimental research conducted by Lui and Astaneh-Asl [24]. In the experimental study conducted by Lui and Astaneh-Asl [24], the moment-resisting capacities of CGFs were investigated using W18×35 (d = 455 mm), W24×55 (d = 602 mm), and W33×118 (d = 856 mm) beams with shear tab connections featuring 4, 6, and 8 bolts, respectively. In the present study, W16×26 (d = 399 mm) and W27×84 (d = 688 mm) beams are employed; therefore, the proposed numerical model to simulate rotational response of the beam-to-column connections in the CGFs including the effects of the composite floor slab is applicable, as it encompasses the section sizes and connection capacities examined by Lui and Astaneh-Asl [24]. Coefficients used in the numerical modeling and comparison moment rotation curves obtained from both numerical and experimental results [24] are given in Figures 7 and 8 respectively. Figure 8 indicates reasonable agreement between the numerical model and experimental results.

The contribution of out-of-plane rigidity of the composite slab to the stiffness and strength of links in EBFs was investigated by Ricles and Popov [44] and Ioan et al. [9]. Research following the 2010 and 2011 New Zealand earthquakes suggested the out-of-plane rigidity

of the composite slab at the EBF links contributed to a reduction in residual drift [4, 6]. Ricles and Popov [44] reported that links with a composite slab show an increase in shear yield strength by 3%, maximum shear strength by 8% and elastic stiffness by 24% relative to links without a composite slab. Similarly, Ioan et al. [9] reported that composite slab increases shear yield strength by 7%, elastic stiffness by 5% and post-yielding stiffness by 18%. In this study, to consider the contribution of the composite slab to seismic response of the EBF, shear yield strength, elastic stiffness and post-yielding stiffness of the link members were increased by 7%, 5% and 18% respectively.

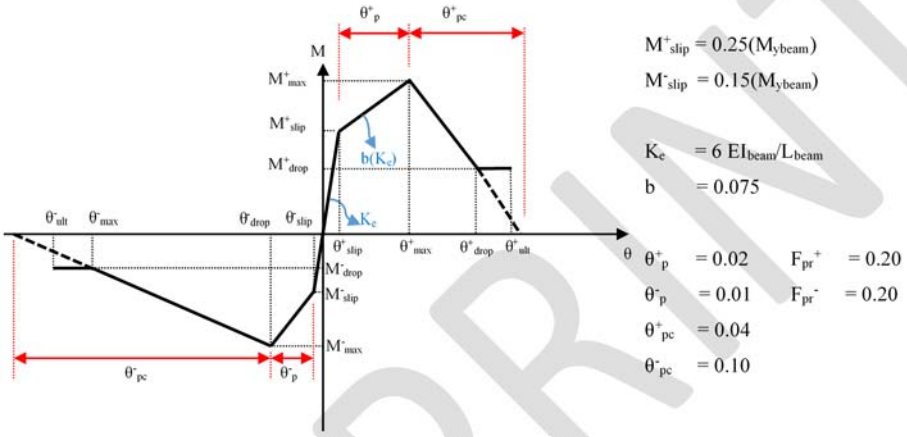

Figure 7 - Coefficients used in the "Modified Ibarra-Medina-Krawinkler Deterioration Model with Pinched Hysteretic Response" for the gravity frame connections

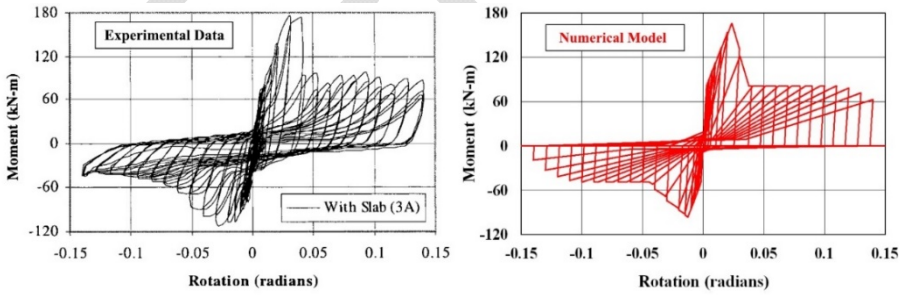

Figure 8 - Comparison of the numerical models and experimental results of the shear tab connection with a composite floor slab conducted by Lui and Astaneh-Asl [24]

4. SELECTION AND SCALING OF THE GROUND MOTIONS

All models were subjected to scaled and unscaled 44 far-field ground motions defined in FEMA P695 [35]. Ground motions were scaled based on the risk-targeted maximum considered earthquake (MCER). As stated in NIST Technical Note 1863-3 [33], the seismic design category was selected as Dmax and site class was selected as D. Building risk category

was taken as II. Spectral response acceleration parameters at short periods, SS and at a period of 1 second, S1 are 1.50g and 0.60g respectively. For Site Class D, the short-period site coefficient is 1.00 and the 1-second site coefficient is 1.50. The MCER and design spectral response acceleration parameters at short periods and a period of 1 second are given as follows.

$$S_{MS}=1.50g, \quad S_{M1}=0.90g, \quad S_{DS}=1.00g, \quad S_{D1}=0.60g \tag{1}$$

Scaling of the ground motions was performed similar to ASCE 7 [36] recommendations with minor changes. Scaling coefficients were calculated separately for each archetype having different numbers of stories. First, T_{avg}, the average of the natural periods of the archetypes designed based on ELF and RSA were calculated. Then, the error between S_a from the response spectrum for the ground motion and Sa from the design response spectrum based on the MCE_R were computed for the range between $0.2\times T_{avg}$ and $1.5\times T_{avg}$ at each 0.01 sec interval. After that, the response spectrum from each ground motion was scaled to obtain a minimum error giving the first scaling factor. After computing the first scale factor, the average response spectrum from the scaled ground motions were calculated for the 44 far-field ground motions. Then, the response spectrum from each scaled ground motion was scaled again for each ground motion record set such that no Sa value from the response spectrum based on the ground motion is lower than that from the response spectrum based on the MCE_R between $0.2\times T_{avg}$ and $1.5\times T_{avg}$ at each 0.01 sec giving the second scaling factor. Finally, the scale factors given in Table 3 were obtained by multiplying the first and second scale factors. A representative acceleration response spectrum under the mean of unscaled and scaled ground motions based on MCE_R for ME4 is given in Figure 9. In addition to scaled ground motions, unscaled ground motions were also used in this study is to investigate the seismic response of the EBF under real earthquakes. As shown in Figure 9, the mean of the unscaled response spectra is lower by nearly 55%, 69%, and 69% than the design basis earthquake (*DBE*) for ME4, ME8, and ME16 respectively.

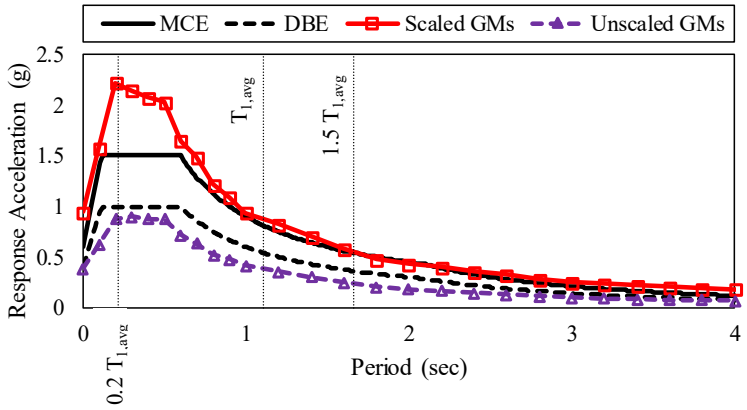

Figure 9 - Acceleration response spectra under the mean of unscaled and scaled ground motions based on MCE_R for ME4.

Table 3 - Scale factors of the ground motions defined in FEMA P695 [35]

Set no	Scale Factors				Set no	Scale Factors		
	ME4	ME8	ME16			ME4	ME8	ME16
1	1.281	1.658	2.110		23	3.425	5.414	4.154
2	1.155	1.638	2.290		24	1.906	3.047	3.452
3	2.181	2.124	2.584		25	1.452	2.390	3.349
4	1.822	2.548	3.011		26	2.272	3.798	4.973
5	1.457	1.743	1.780		27	2.759	4.372	4.215
6	1.266	1.742	2.133		28	2.398	2.119	2.313
7	3.066	3.741	3.595		29	2.576	2.643	2.321
8	2.028	2.397	2.708		30	1.921	1.430	1.461
9	3.284	2.583	2.181		31	2.425	2.695	2.496
10	2.307	2.279	1.895		32	3.321	2.171	2.035
11	2.721	2.388	2.359		33	2.677	2.802	3.206
12	2.817	3.500	2.878		34	3.105	2.795	2.722
13	2.048	2.679	3.526		35	2.100	2.953	3.686
14	2.333	2.888	3.055		36	1.976	3.824	4.667
15	2.772	2.875	3.283		37	2.536	1.341	0.938
16	2.904	3.695	4.099		38	1.596	1.127	0.637
17	2.599	2.001	1.291		39	2.578	3.862	3.423
18	1.595	1.733	1.748		40	2.428	3.356	4.009
19	8.531	8.362	6.688		41	3.907	4.135	2.767
20	7.063	5.695	2.545		42	7.543	6.718	5.250
21	2.235	2.337	1.960		43	3.651	6.000	7.584
22	3.461	3.769	2.661		44	2.903	5.099	6.201

5. ANALYSIS RESULTS AND EVALUATION

44 far-field ground motions defined in FEMA P695 [35] were applied to Model A and B. Ground motions were considered as both unscaled as well as scaled based on MCE_R. After each nonlinear analysis, maximum interstory drift ratios, residual drift ratios and maximum link rotation angles were collected and the mean of these values are presented herein.

5.1. Interstory Drift Ratio

The distributions of interstory drift ratios of the archetypes over their height are depicted in Figure 10. The mean of the maximum interstory drift ratios for Model A under unscaled ground motions are 0.87%, 1.01%, 0.71% for the 4, 8 and 16 story archetypes designed based on ELF whereas they are 0.75%, 1.09%, 0.84% for the archetypes designed based on RSA.

For Model B, these values decrease to 0.69%, 0.84%, 0.59% for the archetypes designed based on ELF and 0.73%, 0.95%, 0.74% for the archetypes designed based on RSA.

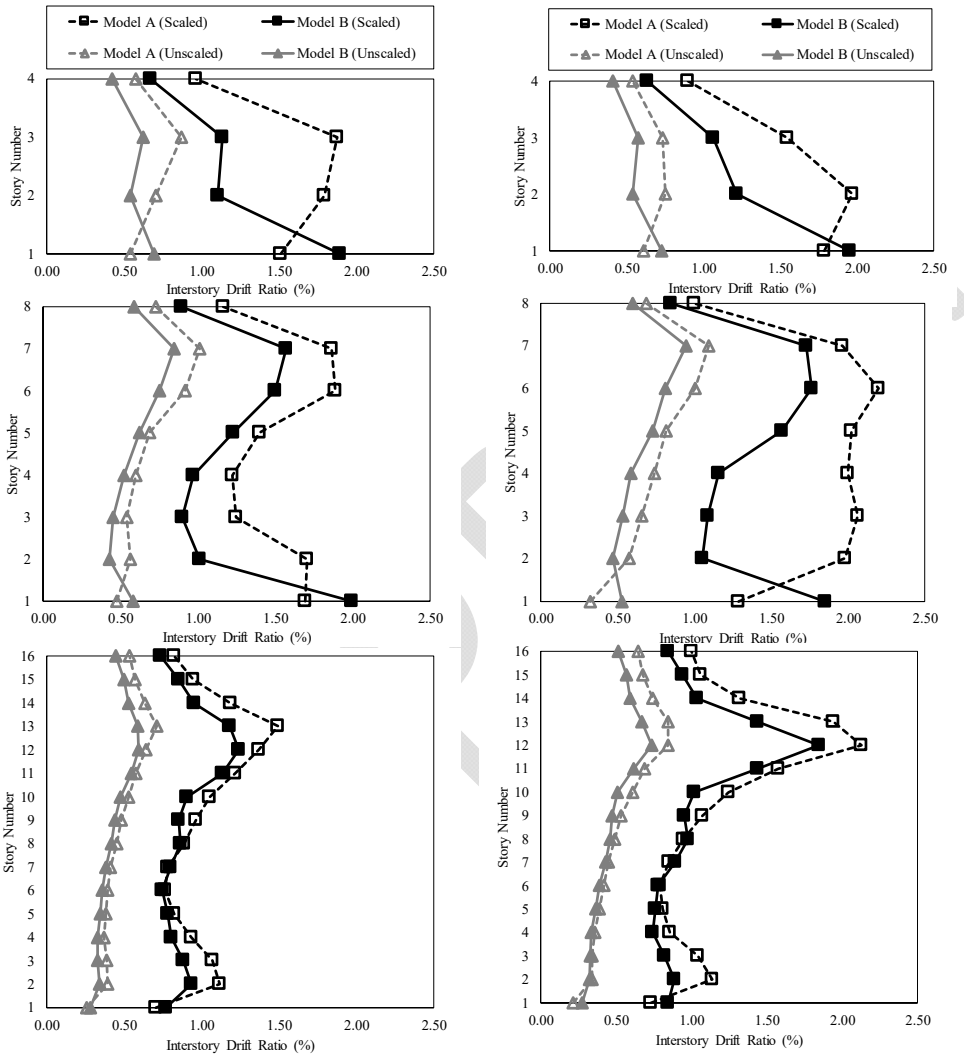

(a) (b)

Figure 10 - Mean of the maximum interstory drift ratios of the archetypes designed based on (a) ELF and (b) RSA

The mean of the maximum interstory drift ratios for Model A under scaled ground motions are 1.88%, 1.88%, 1.49% for the 4, 8 and 16 story archetypes designed based on ELF, and 1.97%, 2.20%, and 2.18% for the archetypes designed based on RSA. For Model B, the mean

of maximum interstory drift ratios are 1.89%, 1.99%, and 1.24% for the archetypes designed based on ELF and 1.95%, 1.85%, 1.84% for the archetypes designed based on RSA.

As expected, the archetypes have larger interstory drift ratios for scaled versus unscaled ground motions. The maximum interstory drift ratios for the Models A and B under unscaled ground motions are 1.09% and 0.95% respectively whereas these values under scaled ground motions are 2.20% and 1.99%. Therefore, the maximum interstory drift ratios under scaled ground motions are approximately double those under unscaled ground motions. The results also indicate that the maximum interstory drift ratios are generally greater for prototypes designed using RSA compared to those designed using ELF. This was the cases both for Models A and B and both for unscaled and scaled ground motions. Further, the differences were most notable for the 8 and 16 story archetypes. As indicated by Table 1, the archetypes designed using RSA had lighter beams, links and columns at many stories compared to the archetypes designed using ELF, likely explaining the differences in maximum interstory drift ratios.

As mentioned in Section 2, although the base connections of the columns forming the EBFs are fixed, those of the columns forming the CGFs are pinned. Since this configuration changes the dynamic characteristics of the archetypes, it leads to an increase in the first story lateral displacements of Model B, in which the effect of the CGFs is considered, and consequently results in higher interstory values only at the first story compared to Model A. For either scaled or unscaled ground motions, the maximum interstory drift ratios for Model B were about 10% less than for Model A. Including the CGFs composed of GFs and the effects of the out-of-plane rigidity of the composite slab in the models therefore reduced maximum interstory drift ratios, although not by a significant amount.

5.2. Residual Drift Ratio

In the analyses, the archetypes were allowed to respond in free vibration for 120 seconds after the ground motion records ended. The residual drift ratio of the EBF was recorded after that time. In addition, to investigate how EBFs respond during the replacement of the damaged links, dynamic analyses were conducted after removal of the damaged links from the EBF. Removal of the damaged links was accomplished by using the "remove" command defined in Opensees [34]. The actual sequence in which links would be removed and replaced over the height of the frame following an earthquake may be quite variable depending on damage patterns, the need to maintain building safety during the replacement process, and economic factors. To provide a preliminary indication of the effects of the link removal process and to simplify the analysis, all links over the height of the EBFs were removed simultaneously in this study. As shown in Figure 11, another 120 seconds were added to the analyses to provide damping of EBFs after removal of the links. Distribution of the residual drift ratios of the archetypes over the height are shown in Figure 12.

The mean of the residual drift ratios for Model A for the 4, 8 and 16 story archetypes designed based on ELF under scaled ground motions were 0.61%, 0.84%, 0.33% respectively. For Model B, these values reduce to 0.45%, 0.56%, 0.19%. After removal of the damaged links these values further decrease to 0.38%, 0.38%, 0.12% which indicates how the damaged buildings try to re-center when the damaged links are removed. The mean of the residual drift ratios for Model A designed based on RSA under scaled ground motions are 0.82%, 1.05%,

and 0.81% for the 4, 8, and 16 story archetypes. For Model B these values reduce to 0.46%, 0.60%, and 0.40%. After the removal of the damaged links, these values further reduce to 0.38%, 0.22%, and 0.34% which are below the 0.5% residual drift limit suggested to maintain the functionality of the buildings as well as avoid human discomfort [17]. As shown in Figure 11, however, the changes in the amount of the residual drift do not occur evenly over the heights after the removal of the damaged links.

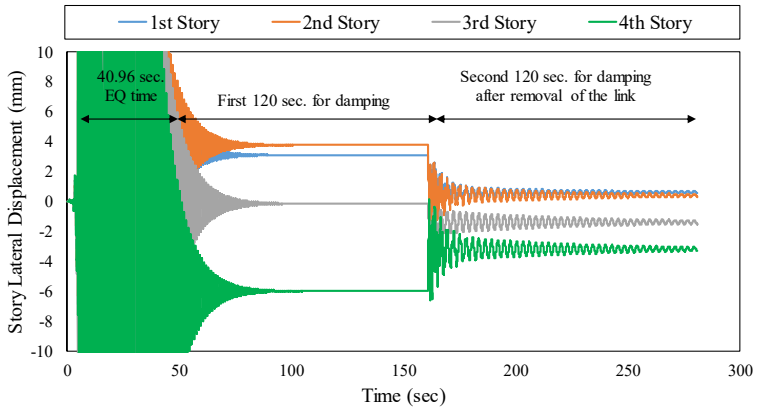

Figure 11 - Story lateral displacement variation over time of ME4 designed based on RSA under 1995 Kobe, Japan EQ record from Nishi-Akashi station (NIS000)

The mean of the residual drift ratios for Model A designed based on ELF under unscaled ground motions are 0.14%, 0.14%, 0.08% for the 4, 8 and 16 story archetypes. For Model B, these values decrease to 0.09%, 0.07%, and 0.04%. On the other hand, the mean of the residual drift ratios for Model A designed based on RSA under unscaled ground motions for the 4, 8 and 16 story archetypes are 0.13%, 0.15%, 0.15% respectively whereas for Model B these values reduce to 0.10%, 0.09%, and 0.07%.

According to the results obtained from these numerical analyses, residual drift ratios of the archetypes under the unscaled ground motions are about 40% of the residual drift ratios under the scaled ground motions. Moreover, the residual drift ratios of the archetypes designed based on ELF were about 75% of the residual drift ratios of the archetypes designed based on RSA. The residual drift ratios for Model B were about 60% of the residual drift ratios for Model A. In addition, after removal of the damaged links these values further decreased. Overall, the residual drift ratios for Model B after link removal are about 40% of the residual drift ratios for Model A.

The residual drift for EBFs determined in this numerical study is significantly lower than that reported from numerical studies on special moment resisting frames (SMFs) and buckling restrained brace frames (BRBFs) [32]. As reported in the study conducted by Erochko et al. [32], the mean of the residual drift ratios varied between 2.0-4.0% for SMFs and 2.0-5.0% for BRBFs under scaled ground motions based on MCE. On the other hand, according to this study, the mean of the residual drift ratios under scaled ground motions based on MCE is 1.05% for Model A and 0.60% for Model B. This value further decrease to 0.38% after

removal of the damaged links. Even without link removal, these results suggest significantly better behavior of EBFs compared to SMFs and BRBFs in terms of residual drift.

The favorable behavior of EBFs with respect to residual drift may, in part, be due to the high degree of strain hardening exhibited by shear links. The ultimate strength of a shear link is, on average, 40-percent higher than the initial shear yielding strength [40]. A study conducted on the residual drift of BRBFs [45] showed that even a small increase in strain hardening resulted in a significant reduction in residual drift.

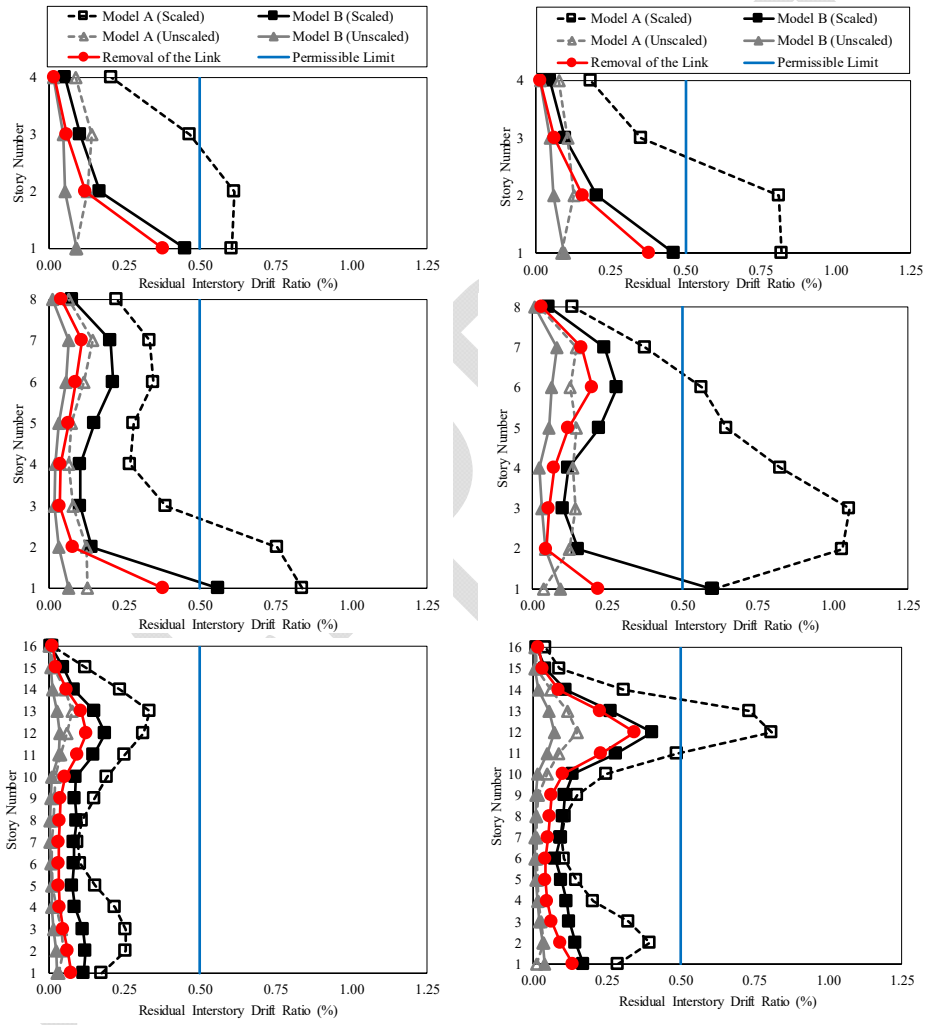

(a) (b)

Figure 12 - Mean of the residual drift ratios of the archetypes designed based on (a) ELF and (b) RSA

5.3. Link Rotation Angle

The mean of the maximum link rotation angles of Models A and B are plotted in Figure 13 for the archetypes designed based on ELF and RSA. The mean of the maximum link rotation angles for Model A under unscaled ground motions are 0.05, 0.04, 0.02 rad for the 4, 8 and 16 story archetypes designed based on ELF. These values are 0.04, 0.05, 0.03 rad for the archetypes designed based on RSA. The mean of the maximum link rotation angles for Model B under unscaled ground motions are 0.03, 0.03, 0.02 rad for the archetypes designed based on ELF and 0.04, 0.03, and 0.02 rad for the archetypes designed based on RSA.

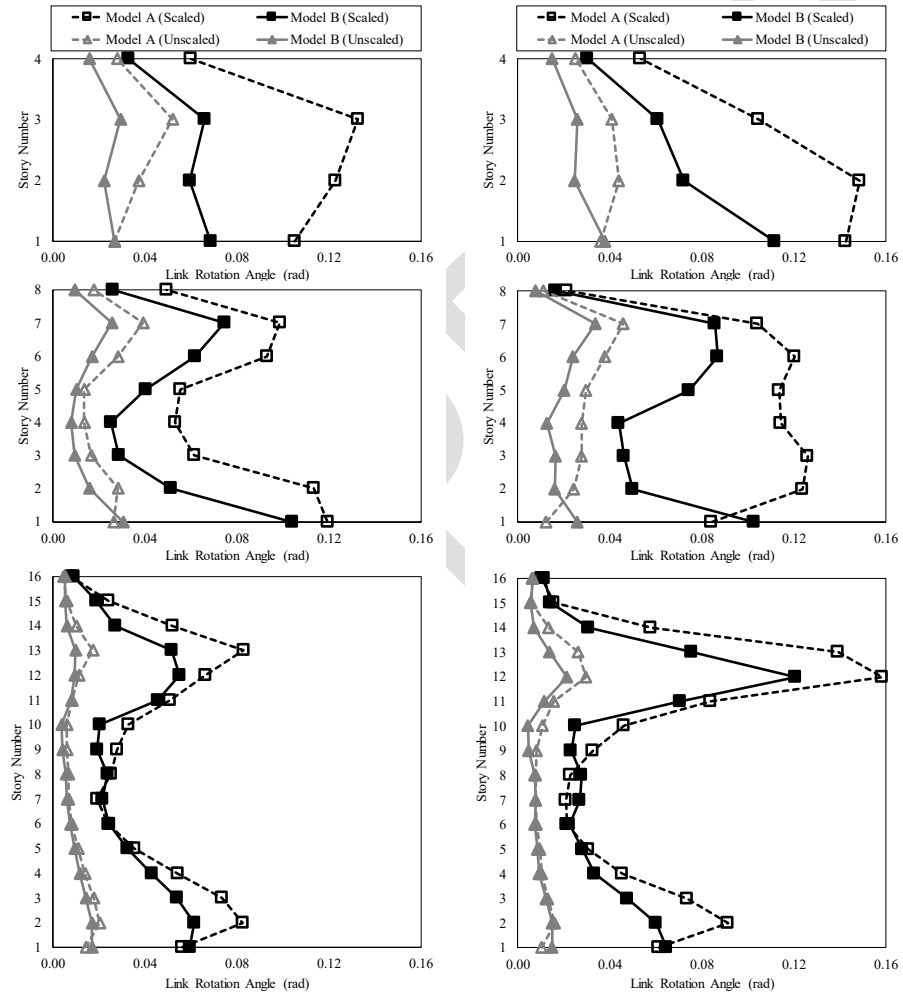

(a) (b)

Figure 13 - Mean of the maximum link rotation angles of the archetypes designed based on (a) ELF and (b) RSA

The link rotation angles increase significantly for the archetypes under scaled ground motions. The mean of the maximum link rotation angles for Model A under scaled ground motions are 0.13, 0.12, 0.08 rad for the 4, 8 and 16 story archetypes designed based on ELF. These values are 0.15, 0.13, 0.16 rad for the archetypes designed based on RSA. The mean of the maximum link rotation angles for Model B under scaled ground motions are 0.07, 0.10, 0.06 rad for the 4, 8 and 16 story archetypes for archetypes designed based on ELF and 0.11, 0.10, 0.12 rad for archetypes designed based on RSA. For both Models A and B, the maximum link rotation angles were approximately double for the 16 story archetype designed based on RSA compared to the 16 story archetype designed using ELF.

As discussed earlier, the numerical model used for the links did not simulate link fracture, which may be expected to occur for link rotations beyond approximately 0.10 to 0.12 rad [40]. Link rotation angles exceeding these values were predicted for Model A designed using RSA and subjected to the scaled ground motions. Consequently, the maximum interstory drift ratios may well be greater than predicted by the analyses. For Model B designed using RSA and subjected to scaled ground motions, the link rotations were significantly reduced and were 0.12 rad or less. This indicates that the CGFs composed of GFs and the effect of the out-of-plane rigidity of the composite slab on the EBF links provided a significant safety benefit to the archetypes when designed using RSA.

For Model A and B archetypes designed using ELF, the link rotation angles were all below 0.12 rad for both unscaled and scaled ground motions. The only exception to this was the 4-story Model A archetype under scaled ground motions, where the mean of the maximum link rotation angle reached approximately 0.14 rad. This observation reinforces previous results showing better performance for designs based on ELF compared to designs based on RSA.

5.4. Residual Link Rotation Angle

Residual link rotation angles were determined after the archetypes were completely damped by applying the similar methodology mentioned in residual drift calculation. The distributions of the residual link rotation angles over the height of the archetypes are shown in Figure 14.

The mean of the residual link rotation angles for Model A under scaled ground motions are 0.04, 0.05, 0.03 rad for the 4, 8 and 16 story archetypes designed based on ELF. These values increase to 0.05, 0.06, 0.06 rad for the archetypes designed based on RSA. The mean of the residual link rotation angles for Model B where GFs and composite slabs were considered decrease to 0.01, 0.02, 0.02 rad for the archetypes designed based on ELF and 0.02, 0.03, 0.03 rad for the archetypes designed based on RSA. The mean of the residual link rotation angles are all below 0.01 rad for unscaled ground motions.

Larger residual link rotations may impact the serviceability of a building after an earthquake. The permanent relative displacement of the link ends can be estimated as the residual link rotation multiplied by the link length. For example, for the 16 story archetype, the link length is 991mm (39 in.). A residual link rotation of 0.06 rad results in a relative link end displacement of 59 mm (2.3 in.). This relative link end displacement will cause permanent vertical distortion of the floor slab, impacting the useability of the building, and may be costly to repair. The significantly smaller residual link rotations for the Model B archetypes

compared to the Model A archetypes suggests a significant post-earthquake benefit of the composite gravity framing.

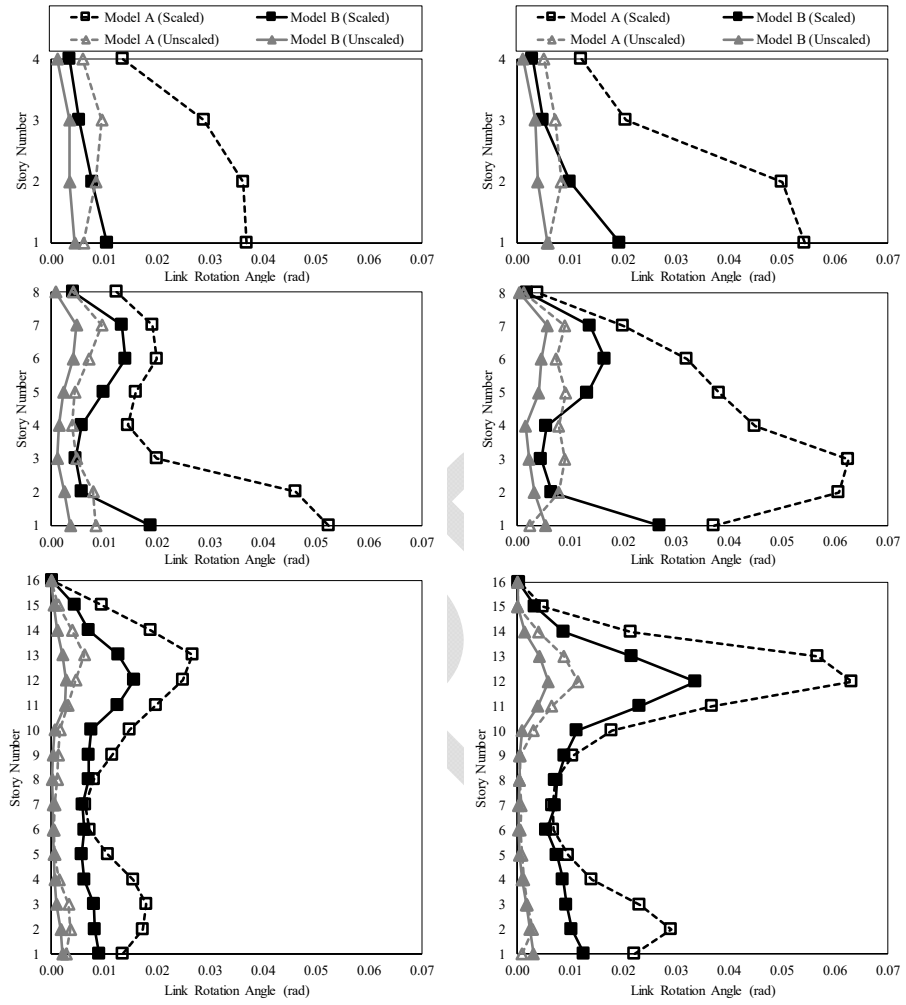

(a) (b)

Figure 14 - Mean of the residual link rotation angles of the archetypes designed based on (a) ELF and (b) RSA

5.5. Characteristics of the Composite Gravity Framing that Lead to Lower Residual Drift and Residual Link Rotation Angle

The analyses described above indicate that the composite gravity framing significantly reduced the residual drift and the residual link rotation angles of the EBF archetypes. To further investigate this result, the 4-story archetype designed based on ELF was further

analyzed under six ground motions, scaled based on MCE_R, selected arbitrarily among the 44 ground motions considered in this study. Four models were considered, as follows:

- The bare steel EBF model (Model A).
- An EBF model with GFs (Model A – GFs). The model included the composite gravity frames, including the beneficial effects of the flexural resistance of the beam to column gravity connections as well as the beneficial effects of the continuity of the gravity columns over the height of the frame.
- An EBF model including only the contribution of the out-of-plane rigidity of the composite slab to the stiffness and strength of links (Model A - CS). This model did not include any of the gravity frames.
- The EBF model including the GFs and the contribution of the out-of-plane rigidity of the composite slab to the strength and stiffness of the links (Model B).

The mean of the maximum drift ratios, the mean residual drift ratios as well as the mean of the maximum link rotation angles and the mean residual link rotation angles are plotted in Figure 15.

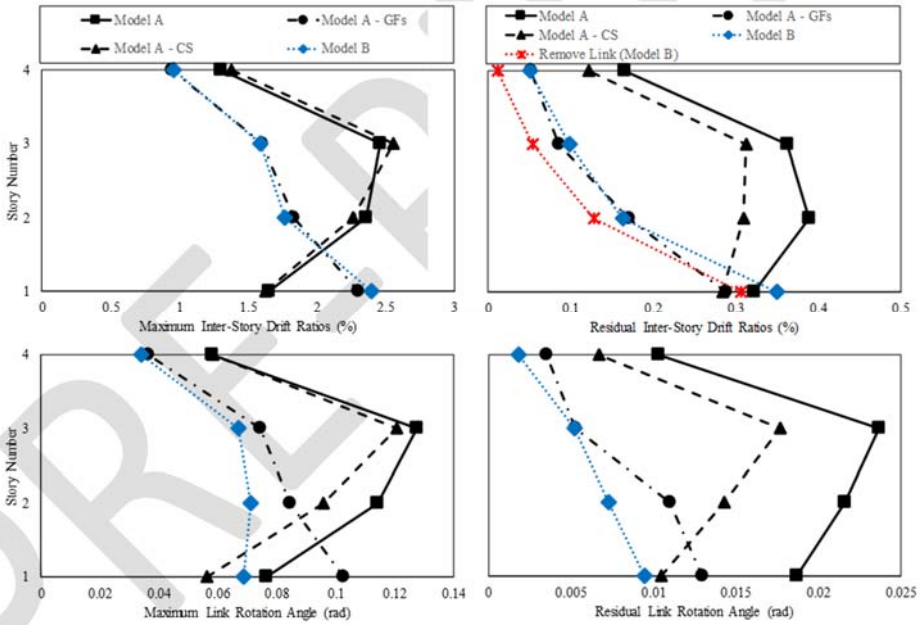

Figure 15 - Effect of the composite gravity frames and out-of-plane rigidity of composite slab on seismic response of the archetypes

According to the analysis results, the GFs (Model A – GFs) reduced the maximum and residual link rotation angle by 20% and 46% respectively of the archetype when compared to the bare EBF (Model A). On the other hand, the effect of out-of-plane rigidity of the composite slab on link strength and stiffness (Model A – CS) decreased the maximum link

rotation angle by 5% and residual drift angle by 25%. When CGFs composed of GFs and out-of-plane rigidity of the composite slab were considered at the same numerical model (Model B), these reductions of the maximum and residual link rotation angle reached up to 45% and 63%.

As for maximum interstory drift and residual drift ratios, while the out-of-plane rigidity of the composite slab (Model A – CS) did not affect the maximum interstory drift ratios, it contributed to decreasing the residual drift ratios by 20%. On the other hand, the GFs (Model A – GFs) changed the interstory drift pattern along the height of the archetype. The existence of the GFs reduced the maximum and residual drift ratios by 7% and 26% of the archetype respectively when compared to bare EBF (Model A). The residual drift ratio of the archetype in Model B was 10% lower than that of the archetype in Model A. However, Model B produced a 22% greater maximum residual drift ratio in the first story compared to Model A-CS, which may be attributed to the change in the dynamic response of the archetype when GFs were added to the numerical model. Furthermore, when the damaged link was removed from the numeric model, the residual drift ratio further decreased by 12%.

6. CONCLUSIONS

In this study, the effects of CGFs on the seismic behavior of EBFs were investigated. Scaling of the ground motions, seismic load calculation methods and the number of stories were considered as the variables. In addition, the amount of residual drift ratio and reduction of residual link rotation angle resulting from the removal of the damaged links was also examined. Key findings obtained from the results of this study are as follows.

- Including the CGFs composed of GFs along with out-of-plane composite floor effects in the models (Model B) showed only a small reduction in the maximum interstory drifts compared to the models that included only the bare steel EBF (Model A). However, the models that included the CGFs showed the maximum link rotation angles reduced by 25% and the residual drift ratios reduced by 40% compared to the models that included only the bare steel EBF. Thus, the CGFs consisting of the GFs and the composite floor effects have a significant beneficial effect on performance.
- Past research has suggested that residual drifts of up to 0.5% may be acceptable following an earthquake based on maintaining building functionality, safety and occupant comfort. Based on this study, even when subjected to ground motions scaled to the MCE, many of the archetypes showed residual drifts less than 0.5% when the beneficial effects of the CGFs composed of the GFs and the composite slab on EBF link response were included in the model. This suggests that even when subjected to very severe earthquake ground motions, many buildings constructed with EBFs may not have excessive residual drifts and therefore could be good candidates for structural repair. Replacement of damaged links may be necessary following an earthquake, and such repairs could be facilitated by adopting EBF designs incorporating replaceable links. Further, the process of removing links for replacement may provide additional benefits in allowing further reductions in residual drift.
- Simulating removal of the damaged links showed a beneficial reduction of residual drift. Link removal was simulated in a very simple manner in this study, by removing all links

simultaneously. Despite this simplification, these results suggest that removal and replacement of damaged links following an earthquake may allow some degree of re-centering to occur. Further research examining different patterns of link removal and replacement would be beneficial to further understand the influence of link removal on residual drift.

- The archetypes designed based on the ELF method generally show better performance compared with the archetypes designed based on the RSA method. This better performance included smaller interstory drift ratios, smaller link rotation angles, and smaller residual drifts for the archetypes designed based on ELF. The ELF designs generally required larger member sizes than the RSA designs, and the resulting increased strength likely explains the better performance. Based on these results, a re-evaluation of the limits on the use of ELF in ASCE-7 may be warranted.

Symbols

A : Archetypes

b : Strain hardening ratio

$CR1$: Parameter to control the transition from elastic to plastic branches

$CR2$: Parameter to control the transition from elastic to plastic branches

DBE : design basis earthquake

e : Link length

L : bay width of EBF

MCE_R : Risk-targeted maximum considered earthquake

M_p : Plastic moment capacity of the link

$R0$: Parameter to control the transition from elastic to plastic branches

S : Story number

S_a : *Elastic* spectral response acceleration parameter

S_{DS} : Design spectral response acceleration parameter at short periods

S_{D1} : Design spectral response acceleration parameter at a period of 1 s.

S_{MS} : MCE_R spectral response acceleration parameter at short periods

S_{M1} : MCE_R spectral response acceleration parameter at a period of 1 s.

T_{avg} : Average of the natural periods

V_p : Plastic shear capacity of the link

ρ : Link length ratio

Acknowledgements

The study was supported by the Scientific and Technological Research Council of Turkey (TÜBİTAK) under the grant number TÜBİTAK 2219-1059B191700103. The authors thank to TÜBİTAK for their supports. The opinions expressed in this paper are those of the authors and do not reflect the views of the sponsor.

References

[1] AISC, "Seismic Provisions for Structural Steel Buildings – ANSI/AISC 341-22," American Institute of Steel Construction, Chicago, Illinois, 2022.

[2] Kazemzadeh Azad, S.and Topkaya, C. (2017). A review of research on steel eccentrically braced frame. Journal of Constructional Steel Research, vol. 2017, no. 128, pp. 53-73.

[3] Clifton, C.C., Bruneau, M., MacRae, G., Leon R. and Fussell, A. (2011). Steel structures damage from the Christchurch earthquake series of 2010 and 2011. Bulletin of the New Zealand Society for Earthquake Engineering, vol. 44, no. 4, pp. 297-318.

[4] Clifton, C.C., Nashid, H., Ferguson, G., Hodgson, M., Seal, K. S., MacRae, G. A. and Gardiner, S. (2012). Performance of Eccentrically Braced Framed Buildings In The Cristchurch Earthquake Series of 2010/2011. 15th World Conference on Earthquake Engineering 2012 (15WCEE) , Lisbon, Portugal.

[5] Ramsay, J. J., Fussell, A. and Wilkinson, R. G. (2013). Design of replaceable-link eccentric braced frames in postearthquake Christchurch. Proceedings of the Steel Innovations Conference 2013, Christchurch, New Zealand.

[6] Gardiner, G., Clifton C.C. and MacRae, G. A. (2013). Performance, damage assessment and repair of a multistorey eccentrically braced frame building following the Christchurch earthquake series, steel innovations conference 2013. Proceedings of the Steel Innovations Conference 2013, Christchurch, New Zealand.

[7] Stratan, A., Dubina D. and Dinu, F. (2003). Control of global performance of seismic resistant EBF with removable link. Proceedings of the 4th International Conference on Behaviour of Steel Structures in Seismic Areas (STESSA 2003), Naples, Italy, 2003, PP. 174-180.

[8] Stratan A. and Dubina, D. (2004). Bolted links for eccentrically braced steel frames. Proceedings of the 5th AISC/ECCS International Workshop: Connections in Steel Structures V. Behaviour, Strength and Design, Delft, The Netherlands, 2004, PP. 223-332.

[9] Ioan, A., Stratan, A., Dubina, D., Poljansek, M., Molina, F.J., Taucer, F., Pegon, P. and Sabau, G. (2016). Experimental validation of re-centring capability of eccentrically braced frames with removable links. Engineering Structures, vol. 113, pp. 335-346.

[10] Balut N. and Gioncu V. (2003). Suggestion for an improved 'dog-bone' solution. Proceedings of the 4th International Conference on Behaviour of Steel Structures in Seismic Areas (STESSA 2003), Naples, Italy.

[11] Mansour, N. (2010). Eccentrically braced frames with replaceable shear links, Toronto, Ontario, Canada: Ph.D. Thesis, Department of Civil Engineering.

[12] Mansour, N., Christopoulos, C. and Tremblay, R. (2011). Experimental validation of replaceable shear links for eccentrically braced steel frames. Journal of Structural Engineering, ASCE, vol. 137, no. 10, pp. 1141-1152.

[13] Ji, X., Wang, Y., Ma, Q. and Okazaki, T. (2015). Cyclic behavior of very short steel shear links. Journal of Structural Engineering, ASCE, vol. 142, no. 2, p. 04015114.

[14] Bozkurt, M.B. (2017). Developing replaceable members for steel lateral load resisting systems, Ankara, Turkey: Doctoral Dissertation, Middle East Technical Univeresity.

[15] Bozkurt, M.B. and Topkaya, C. (2017). Replaceable links with direct brace attachments for eccentrically braced frames. Earthquake Engineering & Structural Dynamics, vol. 46, pp. 2121-2139.

[16] Bozkurt, M.B. and Topkaya, C. (2018) Replaceable links with gusseted brace joints for eccentrically braced frames," Soil Dynamics & Earthquake Engineering, vol. 151, pp. 305-318.

[17] McCormick, J., Aburano, H., Ikenaga, M. and Nakashima, M. (2008). Permissible Residual Deformation Levels For Building Structures Considering Both Safety And Human Elements. The 14th World Conference on Earthquake Engineering, Beijing, China.

[18] Bozkurt, M.B., Kazemzadeh Azad S. and Topkaya, C. (2019). Development of detachable replaceable links for eccentrically braced frames. Earthquake Engineering & Structural Dynamics, pp. 1-22.

[19] Özkılıç, Y.O., Bozkurt M. B. and Topkaya, C. (2021). Mid-Spliced end-plated replaceable links for eccentrically braced frames. Engineering Structures, vol. 237, no. 2021, p. 112225.

[20] Elkady, A. and Lignos, D. G. (2014). Effect of gravity framing on the overstrength and collapse capacity of steel frame buildings with perimeter special moment frames. Earthquake Engineering & Structural Dynamics, vol. 44, pp. 1289-1307.

[21] Ji, X., Kato, M., Wang, T., Hitaka, T. and Nakashima, M. (2009). Effect of gravity columns on mitigation of drift concentration for braced frames. Journal of Constructional Steel Research, vol. 65, pp. 2148-2156.

[22] Astaneh-Asl, A., Nader, M. N. and Malik, L. (1989). Cyclic behavior of double angle connections. Journal of Structural Engineering, ASCE, vol. 115, no. 5, pp. 1101-1116.

[23] Shen, J. and Astaneh-Asl, A. (1999). Hysteretic behavior of bolted-angle connections. Journal of Constructional Steel Research, vol. 51, pp. 201-218.

[24] Lui, J. and Astaneh-Asl, A. (2000). Cyclic testing of simple connections including effects of slab," Journal of Structural Engineering, ASCE, vol. 126, pp. 32-39.

[25] Abolmaali, A., Kukreti, A. R. and Razavi, H. (2003). Hysteresis behavior of semi-rigid double web angle steel connections. Journal of Constructional Steel Research, vol. 59, pp. 1057-1082.

[26] Boston, M. (2012). Reducing Residual Drift in Buckling-Restrained Braced Frames by Using Gravity Columns as Part of a Dual System, Provo, Utah: Brigham Young University BYU ScholarsArchive.

[27] Flores F.X. and Charney, F.A. (2014). The influence of the gravity system framing on the seismic performance of special steel moment frames. 10th U.S. National Conference on Earthquake Engineering, Anchorage, Alaska.

[28] Dubina, D., Stratan A. and Dinu, F. (2008). Dual high-strength steel eccentrically braced frames with removable links. Earthquake Engineering & Structural Dynamics, vol. 37, no. 15, pp. 1703-1720.

[29] Dubina, D., Stratan, A. and Dinu, F. (2011). Re-centring capacity of dual-steel frames. Steel Construction, vol. 4, no. 2, pp. 73-84.

[30] Ioan, A., Stratan, A., Dubina, D. and Taucer F. (2013). Dual-Steel Eccentrically Braced Frames with Bolted Links – Simulation of Safe Removal Proces. Acta Technica Napocensis: Civil Engineering & Architecture, vol. 56, no. 2, pp. 111-118.

[31] Sabau, G., Poljansek, M., Taucer, F., Pegon, P., Molina, F., Tirelli, D., Viaccoz, B., Stratan, A., Chesoan, A. and Dubina, D. (2014). Seismic Engineering Research Infrastructures For European Synergies: Full-Scale Experimental Validation of a Dual Eccentrically Braced Frame with Removable Links (DUAREM). Report EUR 27030, Luxembourg.

[32] Erochko, J., Christopoulos, C., Tremblay, R. and Choi, H. (2011). Residual Drift Response of SMRFs and BRB Frames in Steel Buildings Designed according to ASCE 7-05. Journal of Structural Engineering, vol. 137, no. 5, pp. 589-599.

[33] Harris, J.L. and Speicher, M.S. (2015). NIST Technical Note 1863-3, Assessment of First Generation Performance-Based Seismic Design Methods for New Steel Buildings, Volume 3: Eccentrically Braced Frames. National Institute of Standards and Technology, Gaithersburg, Maryland.

[34] OPENSEES, Version 2.0 User Command-Language Manual, 2009.

[35] FEMA P695, Quantification of building seismic performance factors, Washington, DC: Building Seismic Safety Council for the Federal Emergency Management Agency, 2009.

[36] ASCE/SEI-7-10, "Minimum Design Loads for Buildings and Other Structures," Structural Engineering Institute of the American Society of Civil Engineers, Reston,Virginia, 2010.

[37] AISC, "Specification for Structural Steel Buildings – ANSI/AISC 360-10", American Institute of Steel Construction, Chicago, Illinois, 2010.

[38] Ramadan, T. and Ghobarah, A. (1995). Analytical Model For Shear-Link Behavior. Journal of Structural Engineering, ASCE, vol. 121, pp. 1574-1580.

[39] Richards, P.W. and Uang, C.M. (2006). Testing Protocol for Short Links in Eccentrically. Journal of Structural Engineering, ASCE, vol. 132, no. 8, pp. 1183-1191.

[40] Okazaki, T., Arce, G., Ryu, H.C. and Engelhardt, M.D. (2005). Experimental study of local buckling, overstrength, and fracture of links in eccentrically. Journal of Structural Engineering, ASCE, vol. 131, no. 10, pp. 1526-1535.

[41] AISC, "Seismic Provisions for Structural Steel Buildings – ANSI/AISC 341-02," American Institute of Steel Construction, Chicago, Illinois, 2002.

[42] AISC, "Seismic Provisions for Structural Steel Buildings – ANSI/AISC 341-05," American Institute of Steel Construction, Chicago, Illinois, 2005.

[43] Lignos, D.G. and Krawinkler, H. (2011). Deterioration Modeling of Steel Components in Support of Collapse Prediction of Steel Moment Frames under Earthquake Loading. Journal of Structural Engineering, ASCE, vol. 137, no. 11, pp. 1291-1302.

[44] Ricles, J.M. and Popov, E.P. (1989). Composite Action in Eccentrically Braced Frames. Journal of Structural Engineering, ASCE, vol. 115, no. 8, pp. 2046-2065.

[45] Mahdavipour, M.A. and Deylami, A. (2014). Probabilistic assessment of strain hardening ratio effect on residual deformation demands of Buckling-Restrained Braced Frames. Engineering Structures, vol. 81, pp. 302-308.

[46] Ozkilic, Y.O., Bozkurt, M.B. and Topkaya, C. (2021). Mid-spliced end-plated replaceable links for eccentrically braced frames. Engineering Structures, vol. 237, no. 112225.